Article

Phase Transition and Dynamics of Defects in the Molecular Piezoelectric TMCM-MnCl$_3$ and the Effect of Partial Substitutions of Mn

Francesco Cordero [1,*], Floriana Craciun [1], Francesco Trequattrini [1,2], Simona Ionita [3], Daniel Lincu [3], Raul-Augustin Mitran [3], Victor Fruth [3], Simona Brajnicov [4], Antoniu Moldovan [4] and Maria Dinescu [4]

[1] Istituto di Struttura della Materia-CNR (ISM-CNR), Area della Ricerca di Roma-Tor Vergata, Via del Fosso del Cavaliere 100, I-00133 Roma, Italy
[2] Dipartimento di Fisica, Università di Roma "La Sapienza", p.le A. Moro 2, I-00185 Roma, Italy
[3] Institute of Physical Chemistry, Romanian Academy, Spl. Independentei 202, 060021 Bucharest, Romania
[4] National Institute for Laser Plasma and Radiation Physics (NILPRP), 077125 Magurele, Romania
* Correspondence: francesco.cordero@ism.cnr.it; Tel.: +39-06-4993-4114

Abstract: We present dielectric and anelastic spectroscopy measurements of the molecular piezoelectric TMCM-MnCl$_3$ and TMCM-Mn$_{0.95}$M$_{0.05}$Cl$_3$ (M = Cu, Fe, Ni; TMCM = trimethylchlorometylammonium), whose powders were pressed into discs and bars and deposited as films on Si by Matrix-Assisted Pulsed Laser Evaporation (MAPLE). As in other molecular ferroelectrics, the dielectric permittivity ϵ' drops at the structural transition temperature T_C, below which the number of directions that the polar TMCM molecules visit is reduced, with the formation of ferroelectric domains. Concomitantly, the Young's modulus E starts increasing and the elastic energy loss has a step-like increase, attributable to the motion of the domain walls. Both the dielectric and elastic anomalies indicate the improper character of the ferroelectric transition, where the ordering of the molecular orientations is not driven by the cooperative interaction of their electric dipoles. Below room temperature, at least two thermally activated relaxation processes appear both in the dielectric and anelastic spectra, whose real and imaginary parts measured at several frequencies can be fit with the Havriliak–Negami formula. The microscopic parameters so-obtained indicate that they are due to point defects, and it is argued that they are Cl vacancies and their complexes with TMCM vacancies. The considerable width of these relaxation maxima is explained by the geometry of the hexagonal perovskite structure. The partial substitution of Mn with 5% Ni has little effect on the anelastic and dielectric spectra, while Cu and, especially, Fe cause a large enhancement of the losses attributed to domain wall relaxation, with substantial contributions also above T_C. The condensation of water from the humidity in the powders compacted by cold pressing was observed and discussed. The piezoelectric activity of the films was assessed by PFM.

Keywords: molecular ferroelectrics; halide perovskites; elasticity; dielectric properties; ceramics

1. Introduction

Ferroelectrics are materials that, below the Curie temperature T_C, develop an electrical polarisation and associated strain. Under the bias field associated with the polarisation, the usually small electrostrictive effect, a deformation proportional to the square of an applied electric field, becomes greatly enhanced and almost linear and is called the piezoelectric effect [1]. The piezoelectric effect is, therefore, the generation of deformation under the application of an electric field and also the generation of an electric field under the application of stress. This is amply used in electromechanical actuators and sensors and mechanical energy harvesting. The most-efficient piezoelectrics are perovskite oxides, especially based on PbZr$_{1-x}$Ti$_x$O$_3$ (PZT), where the polarisation is due to off-centring of the Pb^{2+} and Ti^{4+} cations with respect to the network of O$_6$ octahedra, as in other perovskite oxides, e.g., BaTiO$_3$, (Na,K)NbO$_3$, and Na$_{0.5}$Bi$_{0.5}$TiO$_3$ [1]. Due to environmental

concerns regarding toxic lead, solid solutions of the Pb-free perovskites are being explored as substitutes of the PZT-based materials [2], together with other oxides with more complex structures, such as the Aurivillius phases [3,4]. These oxides can be sintered as ceramics or grown as single crystals at temperatures exceeding 1000 °C; they are brittle, and it is impractical to shape them by machining. In applications where flexible piezoelectrics are needed, polymeric materials are used, mostly based on PVDF, but with piezoelectric coefficients two orders of magnitude smaller than the best ceramics.

Recently, molecular solids have been shown to be able to sustain piezoelectric effects comparable to those of ceramics, with a record $d_{33} \sim 1500$ pC/N of $(TMFM)_x(TMCM)_{1-x}$-$CdCl_3$ [5]. This class of crystals is constituted by organic molecules, with or without an inorganic backbone structure, that occupy fixed lattice positions, but are freely rotating at high temperature and freeze under cooling into a preferred orientation. If the molecules have an electric dipole, their ordering creates a polarisation, and additional off-centring of the cations is also possible. The great advantage of this type of material is that it can be synthesised with chemical or mechanochemical methods, which are inexpensive and allow large quantities of materials to be prepared and, for example, be deposited onto substrates of any shape and size.

Many of these molecular materials with piezoelectric properties are perovskite-type ABX_3, where A is a polar molecule with nominal charge +1 or +2, B a metal or a small organic molecule with charge +2 or +1, and X a halide, but also a small molecule with charge −1. The prototypical perovskite structure is formed by a cubic lattice of BX_6 octahedra sharing the vertices, with the A cations in the empty spaces. If the A molecule is too large to fit in the space between the octahedra, a rearrangement of the octahedra into face-sharing columns is possible. The B–X connectivity is broken within the *ab* plane, and the separation between the columns is dictated by the size of the A cations. This is the case of TMCM-CdBr$_3$ [6], whose structure is shown in Figure 1, and similar compounds $(TMYM)MX_3$ with X,Y = F, Cl, Br, I, and M = Cd, Mn. In the symmetric paraelectric phase, the cell is hexagonal, as evidenced in Figure 1c, with disordered orientations of the TMYM molecules, in particular with Y both up and down. Below T_C, the TMYM molecules fix to one or a subset of these orientations, with additional distortions that lower the symmetry. In TMCM-CdBr$_3$ [6] and TMCM-MnCl$_3$ [7], the polarisation is enhanced by an additional shift of the TMCM cations along the *c* axis [6].
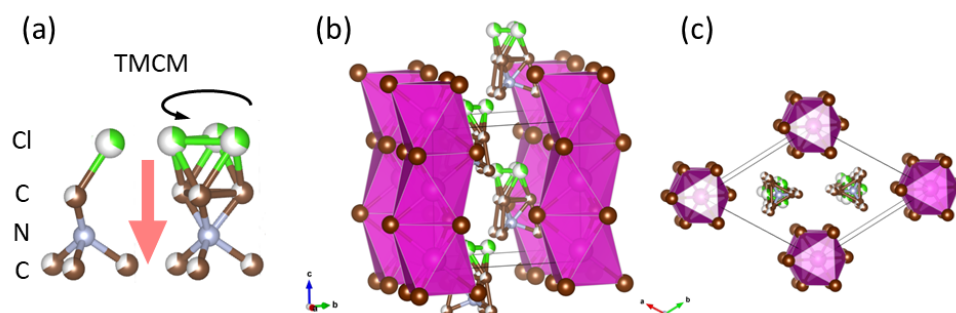
Figure 1. (**a**) TMCM molecule (H atoms not shown) with its electric dipole and a possible fast rotational mode that leaves the electric dipole almost unchanged. (**b**) Structure of TMCM-MnCl$_3$ in the ferroelectric phase, using the CIF files for TMCM-CdBr$_3$ of [6]. (**c**) View of the same structure along the *c* axis.

There are several studies on the many piezoelectric molecular perovskite compounds [5,6,8–11], often as single crystals, but the few dealing with their mechanical properties are first-principles calculations or nanoindentation experiments at room temperature [12], and no attention is paid to the influence of humidity on their properties, a topic that is instead dominant in the field of photovoltaic applications [13–15].

The present study focused on some of the aspects that have been neglected so far, but are relevant to possible large-scale applications, based on films deposited from solution

or other methods or on pressed powders, rather than single crystals. We therefore pressed the powder obtained by chemical methods into bulk samples and also deposited it on Si by Matrix-Assisted Pulsed Laser Evaporation (MAPLE). This method consists of dispersing at a low concentration (5%) the material to be deposited in water, possibly together with other substances to obtain a composite, freezing the liquid and then using it as target for the laser evaporation onto the substrate [16]. This deposition method has several advantages over others: it requires a small amount of material, thanks to the high dilution in the target; it is possible to deposit mixtures of any type of material, including organic molecules; it allows heterostructures to be created. The piezoelectric properties of such films have been assessed by Piezoresponse Force Microscopy (PFM).

With the bulk samples, together with the dielectric properties, it has been possible to measure the dynamic elastic and anelastic properties versus temperature, up to now measured only once in a molecular piezoelectric [17].

We chose TMCM-MnCl$_3$, the first perovskite-type molecular crystal reported to have piezoelectric coefficients comparable to those of PZT [7]. It is closely related to (TMFM)$_x$(TMCM)$_{1-x}$CdCl$_3$, with the highest d_{33} reported so far, but it does not contain Cd and F, which have negative implications on the environment and cost considerations. The highest d_{33} has been obtained exploiting the enhancement of the physical properties of interest, possible in a binary solid solution whose composition–temperature phase diagram has a nearly vertical phase boundary (morphotropic phase boundary) [5,18]. As a first step in that direction, we also prepared TMCM-MnCl$_3$ with 5% of Mn substituted with Cu, Ni, and Fe.

2. Materials and Methods

2.1. Preparation of the Powders

The detailed description of the preparation of the precursor TMCM-Cl and powders of TMCM-MnCl$_3$ undoped and doped with 5% Ni, Cu, and Fe is presented in the Supplementary Information (SI). In brief, TMCM-Cl was synthesised starting from an aqueous solution of trimethylamine and dichloromethane, in acetonitrile at 40 °C for 3 days [7,19]. The solvent was removed under reduced pressure, until a dry white precipitate was formed. The resulting product is highly hygroscopic, and therefore, it was stored under Ar gas and further dried in a vacuum desiccator before use. TMCM-Cl was dissolved in methanol and degassed under Ar flow, and an equimolar amount of anhydrous MnCl$_2$, dissolved in methanol was added dropwise under continuous stirring. The resulting solution was slowly evaporated under a steady flow of Ar for 1 week [7], obtaining pale red crystals.

These crystalline phases were characterised by XRD, FT-IR, TGA, DSC, and DTA, as explained in more detail in the SI. The XRD pattern of the sample containing 5% Ni matches the reported simulated spectra of TMCM-MnCl$_3$ with a *Cc* space group [7], while the other samples display an additional peak at approximately $2\theta = 16°$, presumably from a secondary phase (Figure S2a). Nonetheless, the good incorporation of the dopants in the crystal lattice was demonstrated by the perfect pattern of the Ni-doped phase and by a slight shift towards lower angle values when comparing the Fe- and Cu-doped phases, indicating the changes of the lattice constants upon doping.

All the DSC curves presented the peak from the structural transition at $T_C \sim$397–400 K during heating, in agreement with the dielectric and anelastic measurements.

2.2. Bulk Samples

For the preparation of pressed bulky samples, the powders, when presenting large crystallites, were first crushed into an agate mortar. This treatment produced a paste, due to the humidity promptly absorbed by the material. The paste or uncrushed starting powder was, therefore, dried for several hours in a high vacuum at 60 °C, quickly poured in dies with a 40 × 5 mm shape or circular with a 13 mm diameter, and pressed at 0.3–0.4 GPa for a few minutes into bars and discs with thicknesses of 0.6–0.9 mm. During the few minutes necessary for pouring and levelling the powder in the dies, humidity might be absorbed,

and the pressed sample often was wet and stuck to the pressing pieces, requiring great care for detaching it. When the sample surfaces were wet, they were first dried with mildly warm air, and then, the major surfaces of the discs or the centre of the bars were covered with Ag paint. In some cases, the discs were dried again in a high vacuum, since the dielectric measurements were performed in a sealed small cell. The bars for the anelastic measurements were directly mounted in a high vacuum.

2.3. Dielectric Measurements

Complex dielectric permittivity measurements were carried out over the 120–420 K temperature range at five frequencies between 1 kHz and 1 MHz, using an HP4284A LCR meter with a four-wire probe. The measurements were made during heating and cooling at 1.5–2 K/min in a modified Linkam HFS600E-PB4 stage. The cell is not perfectly air-tight, so that during cooling, the external humidity penetrates and condenses, with subsequent liquefaction and extrinsic dielectric anomalies during heating. In order to prevent this, the Linkam stage was placed into a box continuously flushed with the evaporation of the liquid nitrogen coolant. While preventing the incoming of new humidity, this precaution does not eliminate the presence of water previously absorbed by the sample and difficult to extract with the standard purging of 5 min at 40 °C with the flow of dry N_2.

2.4. Anelastic Measurements

The complex Young's modulus was measured by suspending the bars on thin thermo-couple wires in a high vacuum ($<10^{-5}$ mbar) and electrostatically exciting their flexural resonant modes (Figure S5a in SI). The vibration was detected including the exciting electrode in a resonant circuit at ∼13 MHz, whose frequency was modulated by the change of the sample/electrode capacitance and then demodulated to provide a signal proportional to the sample vibration [20]. The resonance frequency of the fundamental flexural mode is [21]

$$f = 1.028 \frac{h}{l^2} \sqrt{\frac{E}{\rho}} , \tag{1}$$

where l, h, and ρ are the sample's length, thickness, and density. These quantities vary much less than E with temperature and may be assumed to be constant, so that the temperature dependence of Young's modulus is deduced from $E/E_0 = (f/f_0)^2$, where the reference f_0 and E_0 are the resonance frequency and modulus, for example in the high-T phase. The elastic energy loss coefficient, $Q^{-1} = E''/E'$, was measured from the width of the resonance peak or the decay of free oscillations.

2.5. Films

Thin films of TMCM-MnCl$_3$ on the Si substrate were prepared by Matrix-Assisted Pulsed Laser Deposition (MAPLE). This deposition technique was employed due to the possibility to obtain complex architectures of thin films and to avoid organic powder decomposition, which could occur with more energetic techniques. The targets for MAPLE deposition were prepared by mixing TMCM-MnCl$_3$ powders in proportions of 4 wt % with H_2O and successively freezing, under continuous stirring, into a solid sample in liquid nitrogen. The frozen target was placed in the vacuum chamber of the MAPLE setup and irradiated with the beam from a Nd:YAG laser (5 ns pulse duration, 266 nm wavelength, and 10 Hz repetition, Continuum Surelite II, Amplitude Laser Group, Pessac, France). The laser fluence was 480 mJ/cm^2. The obtained plume was composed of water molecules and TMCM-MnCl$_3$ powder particles. The water molecules were pumped away, while the powder particles were deposited on the Si substrate. The obtained thin films showed good continuous coverage, as verified by optical microscopy.

2.6. PFM Measurements

The surface morphology and the local piezoelectric properties of the deposited films were investigated with an Atomic Force Microscope (AFM–XE100, Park Systems, Suwon, Republic of Korea). In the Piezoresponse Force Microscopy (PFM) mode, the local vertical (out-of-plane) mechanical response of the material to an applied electric field was recorded. The local electric field was generated by applying an AC bias from a lock-in amplifier (SR830, Stanford Research Systems, Sunnyvale, CA, USA) to the conductive AFM tip pressed against the surface. The amplitude and phase of the piezoelectric response were extracted from the AFM vertical deflection signal by the same lock-in amplifier. Non-contact AFM imaging and PFM imaging were carried out with NSC14 and NSC36Pt tips, respectively (Mikromasch – Innovative Solutions Bulgaria, Sofia, Bulgaria).

3. Results

3.1. Dielectric Spectra

We present first the dielectric spectrum of TMCM-Mn$_{0.95}$Fe$_{0.05}$Cl$_3$ in Figure 2, because all the relaxation process and other dielectric anomalies are clearly visible. The thermally activated dielectric relaxations are labelled as R1–R4 and are identifiable as peaks in dielectric loss $\tan\delta = \varepsilon''/\varepsilon'$ and steps in the real part ε', which shift to a higher temperature when measured at a higher frequency, as expected from Debye-type relaxations $\Delta\varepsilon \propto (1 + i\omega\tau)^{-1}$ with $\tau(T)$ following the Arrhenius law or, anyway, as a decreasing function of temperature. In fact, the maximum in the imaginary part and the step of the real part are centred at $\omega\tau(T_{\max}) \simeq 1$.
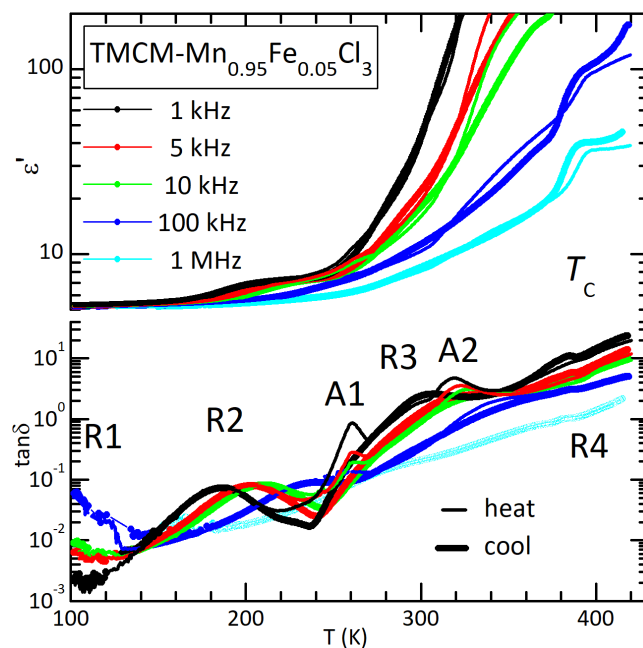

Figure 2. Dielectric permittivity of TMCM-Mn$_{0.95}$Fe$_{0.05}$Cl$_3$ measured during cooling (thick) and subsequent heating (thin) at the frequencies indicated in the legend. The labels Rn indicate thermally activated dielectric relaxations, while An indicate anomalies of other types.

In addition, two peaks in the loss during heating are labelled as A1 and A2, and in some cases, they were also observed during cooling. They shifted little or not at all with varying frequency and were probably extrinsic effects, possibly due to intercalated or adsorbed water. The ferroelectric transition is indicated with T_C and caused a negative step of ε' during cooling and a positive step of $\tan\delta$. Its temperature (upper edge $\simeq 390$ K) agrees with that of the peak in the DSC trace and, for the Fe-doped sample, showed very little hysteresis between heating and cooling.

Figure 3 presents the dielectric curves measured at 10 kHz during cooling for all the TMCM-Mn$_{0.95}$M$_{0.05}$Cl$_3$ samples. They are all consistent with each other, and the major difference is in the amplitude of R3 and also R4, which increased with M in the sequence Mn (undoped), Ni, Cu, and Fe. The undoped and Cu-doped samples also exhibited the anomaly A1 during cooling, whose amplitude for Cu was so large that it appeared also in ε'.
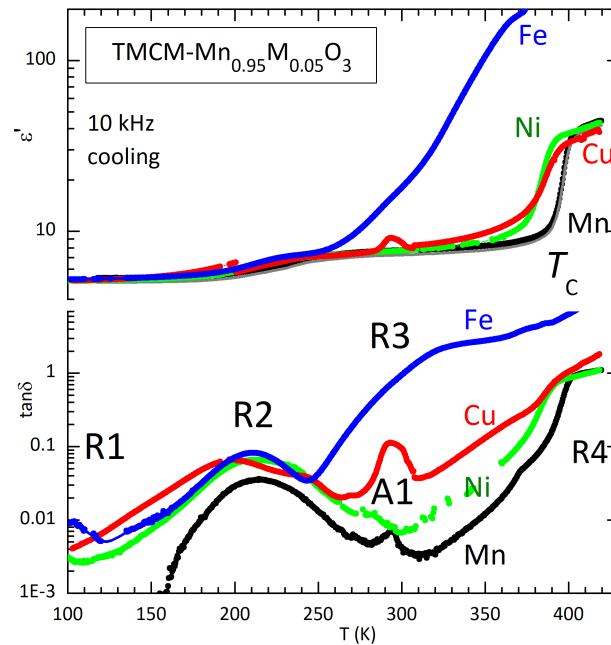

Figure 3. Dielectric permittivity of TMCM-Mn$_{0.95}$M$_{0.05}$Cl$_3$ measured during cooling at 10 kHz. The labels Rn indicate thermally activated dielectric relaxations, while An indicate anomalies of other types.

3.2. Anelastic Spectra

The anelastic measurements where more difficult, since the long and thin bars often broke. In fact, they bent with varying temperature, so that great adjustments of the vertical position of the electrode were necessary, and the initial parallelism between the electrode and sample might be lost. This fact reduced the sample electrode capacity and, hence, the signal, so that, when the electrode was too close to the sample, sparks might arise and damage it (see Figure S5 in Supplementary Materials). Sometimes, the electric contacts to short the thermocouple wires at one edge were lost, requiring a reopening of the system and a deleterious exposure of the sample to humidity, as explained in Section 4.2. We present a few of the several attempts at measuring the anelastic spectra, which were anyway consistent with each other and with the dielectric ones.

Figure 4 presents the anelastic spectrum of TMCM-MnCl$_3$ obtained exciting the first three odd flexural modes during heating and cooling. The real part is presented as the normalised Young's modulus $E(T)/E_0 = [f(T)/f_0]^2$, according to Equation (1), where f_0 was chosen as the resonance frequency in the paraelectric phase. The structural transition produces a gradual, but marked stiffening and a step-like increase of dissipation below T_C. The Q^{-1} curves also reveal the same relaxation processes R2–R4 observed in the dielectric spectra. The sample started irregularly losing stiffness below 270 K and broke below 240 K.
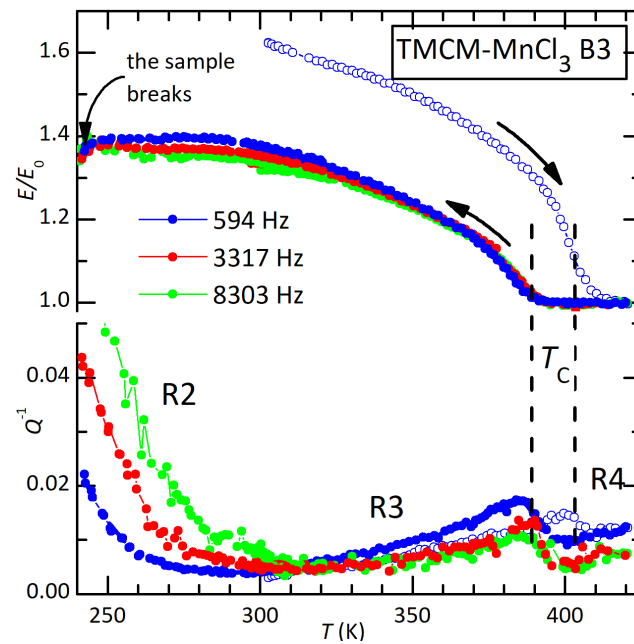
Figure 4. Normalised Young's modulus $E/E_0 = (f/f_0)^2$ and elastic energy loss coefficient Q^{-1} of Sample B3 of TMCM-MnCl$_3$ measured during heating and subsequent cooling, exciting the 1st, 3rd, and 5th flexural modes, whose frequencies at a high temperature are indicated in the legend. The labels Rn indicate the thermally activated relaxations that are observed also in the dielectric spectra.

A more successful measurement down to the lowest attainable temperature was obtained on TMCM-Mn$_{0.95}$Fe$_{0.05}$Cl$_3$ (Figure 5). The anelastic spectrum was very similar to that of the undoped material, but the peak R2 and the tail of R1 could be measured. As in the dielectric spectra, the peak in the losses was accompanied by a step in the real part, whose sign is opposite that of ε', since the elastic modulus is the reciprocal of the susceptibility (compliance).

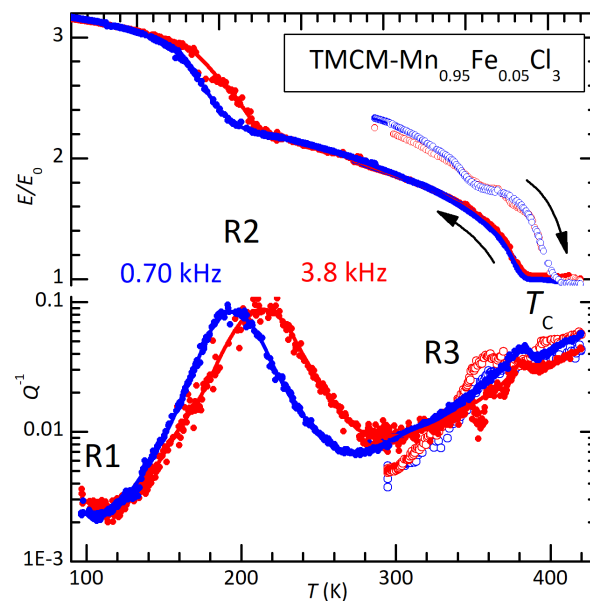**Figure 5.** Normalised Young's modulus $E/E_0 = (f/f_0)^2$ and elastic energy loss coefficient Q^{-1} of Sample B3 of TMCM-Mn$_{0.95}$Fe$_{0.05}$Cl$_3$ measured during heating and subsequent cooling, exciting the 1st and 3rd flexural modes, whose frequencies at high temperature are indicated. The labels Rn indicate the thermally activated relaxations that were observed also in the dielectric spectra.

Figure 6 presents the anelastic spectra of all the TMCM-Mn$_{0.95}$M$_{0.05}$Cl$_3$ compounds measured during cooling, exciting the fundamental resonance. The curves show that R2, R3, and R4 are robust features of these materials, and the substitution of Mn with 5% Ni, Cu, and Fe only changed their amplitudes with little effect on the peak temperatures.
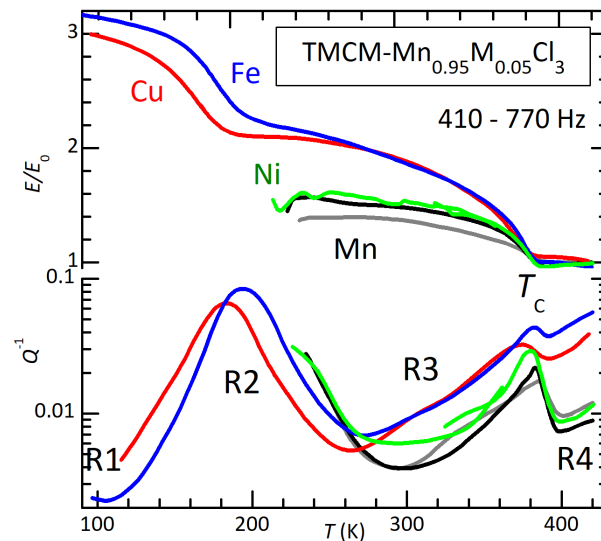

Figure 6. Normalised Young's modulus $E/E_0 = (f/f_0)^2$ and elastic energy loss coefficient Q^{-1} of TMCM-Mn$_{0.95}$M$_{0.05}$Cl$_3$ (M = Mn, Ni, Cu, Fe) measured during cooling exciting the 1st flexural modes, whose frequencies at high temperature are indicated. The labels Rn indicate the thermally activated relaxations that were observed also in the dielectric spectra.

3.3. AFM and PFM Characterisation

AFM topography and PFM images constructed by mapping the out-of-plane phase and amplitude components on a randomly selected area (15 μm × 15 μm) of TMCM-MnCl$_3$ film are shown in Figure 7.
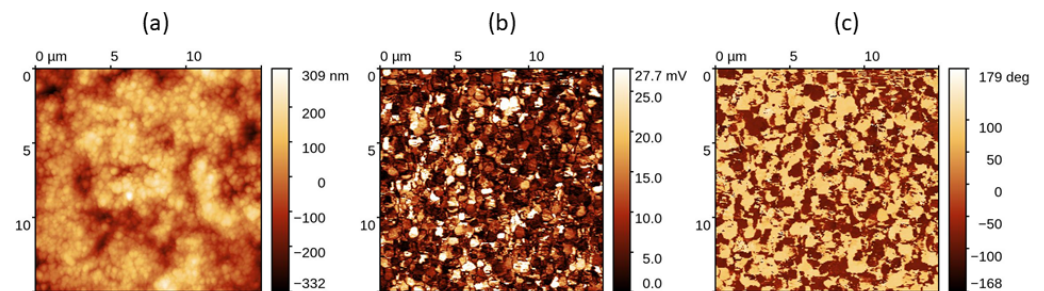

Figure 7. (**a**) Non-contact AFM topography image of TMCM-MnCl$_3$ film, 15 μm × 15 μm. PFM amplitude (**b**) and phase (**c**) images of TMCM-MnCl$_3$ film, 15 μm × 15 μm.

The PFM images show the presence of ferroelectric domains with different out-of-plane polarisation states. The amplitude image (b) indicates the magnitude of the vertical component of the local polarisation. Domains having different amplitudes can be identified, as well as the contours surrounding the domains, where the amplitude is greatly reduced. The phase image (c) shows the orientation of the vertical component of the polarisation: the light/dark contrast indicates opposite orientations.

4. Discussion

The dielectric permittivity of the pressed powder of TMCM-MnCl$_3$ is in agreement with the literature data presented for a single crystal [7]. The step denoting T_C in Figure 3 is at 400 K during cooling, but at 406 K during heating (not shown). The value $\varepsilon' \sim 30$ above

T_C is about half of ε'_c of the single crystal at ≥ 100 kHz because of the random orientation of the crystallites with $\varepsilon'_{ab} \ll \varepsilon'_c$ and indicates that there was very little reduction of the permittivity due to porosity in the pressed powder.

It has already been noted that the step-like dielectric anomalies reveal the improper ferroelectric character of the transition [7]. In fact, in a proper ferroelectric transition, the order parameter is the polarisation, meaning that the transition is driven by the cooperative ordering of the molecular electric dipoles and/or by a polar soft mode. In that case, the dielectric susceptibility presents a Curie–Weiss peak, while the elastic modulus a negative step during cooling [18,22], due to the piezoelectric softening [23,24]. The observed elastic anomaly below T_C is instead a rise of the elastic modulus, coherent with the fact that the transition mainly consists of an ordering of the orientations of the molecular cations, with a consequent drop of the dielectric and elastic susceptibilities. Such an ordering is not driven by cooperative polar interactions, and the formation of polar domains is only a consequence. A similar elastic anomaly has been observed in another molecular ferroelectric, NH_4-$Zn(HCOO)_3$, and explained as due to a dynamics of the order parameter slower than the measuring frequency [17]. In this case, the piezoelectric softening would be hindered even if the polarisation were the order parameter, because it would not be able to follow the applied stress. The gradual stiffening below T_C suggests a proportionality to the square of the order parameter in a nearly second-order transition and might be explained in terms of stronger H bonds between the fraction of ordered cations and the octahedral framework, similar to the cases of NH_4-$Zn(HCOO)_3$ [17] and the tetragonal-to-orthorhombic transition in $MAPbI_3$ (MA = Methylammonium) [25] and $FAPbI_3$ (FA = Formamidinium) [26].

The relaxation processes R1–R4 observed in the anelastic spectra appear as the anelastic counterparts of the dielectric ones. This was more evident for R2, whose temperatures of the maxima as a function of frequency are presented in an Arrhenius plot in Figure 8. The dielectric and anelastic peak temperatures are close enough to be due to the same mechanism.
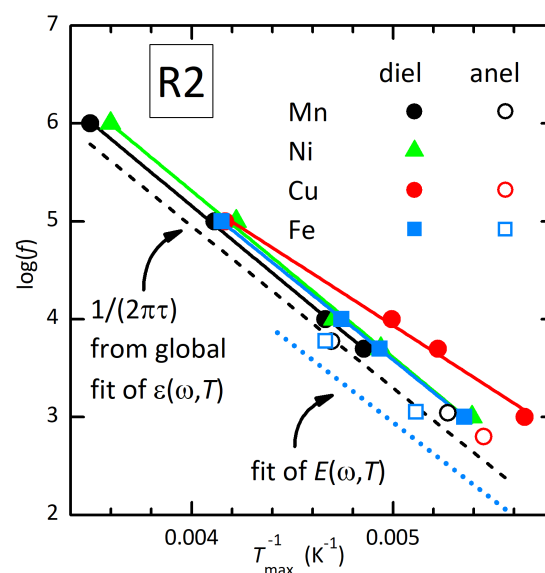
Figure 8. Arrhenius plot of the temperatures of the peaks of $\tan \delta$ and Q^{-1} corresponding to R2. The dashed line is $(2\pi\bar{\tau})^{-1}$ from the global fits of the dielectric spectrum of TMCM-Mn_3 and the anelastic spectrum of TMCM-$Mn_{0.95}Fe_{0.05}Cl_3$.

The partial substitution of Mn with 5% Ni had little effect on the dielectric and anelastic spectra, while Cu and especially Fe caused a large enhancement of the losses labelled as R3 and R4 (Figures 3 and 6). The identical behaviour of dielectric and anelastic relaxations confirmed that they are due the same mechanisms.

For a more stringent assessment of the nature of the relaxation processes, it would be desirable to fit the relaxation curves, but this is quite difficult with so many overlapping

relaxation processes and additional anomalies. We, therefore, concentrated on the dielectric spectrum of undoped TMCM-MnCl$_3$, which is dominated by R2 and R4 well separated apart (Figure 9). From a simple inspection, it is clear that these relaxation processes are characterised by very broad distributions of the relaxation times. In fact, for a pure Debye relaxation, $\varepsilon \propto (1 + i\omega\tau)^{-1}$, the amplitude of the step in the real part is twice the amplitude of the imaginary part and approximately of $\tan\delta$, but the steps of R2 and R4 are instead much larger than twice the corresponding peaks. This is due to the fact that, with a distribution of elementary relaxations with different maximum temperatures, the steps sum up, while the resulting peak is spread with its maximum intensity less than the sum of the heights of the elementary peaks. An expression that can be used to describe both the real and imaginary parts of a broadened relaxation is the Havriliak–Negami formula [27,28]:

$$\varepsilon = \varepsilon_0 + \frac{\Delta\varepsilon}{\left[1 + (i\omega\overline{\tau})^\alpha\right]^\gamma}, \quad (2)$$

which reduces to the Debye formula for $\alpha = \gamma = 1$ and broadens for $\alpha, \gamma < 1$; setting $\gamma = 1$, one obtains the Cole–Cole function. The relaxation time usually follows the Arrhenius law $\tau = \tau_0 \exp(E/T)$. For relaxation between two states with the same energy, the relaxation strength is $\Delta\varepsilon = \Delta/T$ [29], but the intensity of R2 clearly does not decrease with temperature as $1/T$, so that we introduced an average asymmetry A in energy between the initial and final state, which modifies the relaxation strength and rate as [30,31]

$$\overline{\tau}^{-1} = \tau^{-1} \cosh(A/2T)$$

$$\Delta\epsilon = \frac{\Delta}{T \cosh^2(A/2T)} \quad (3)$$
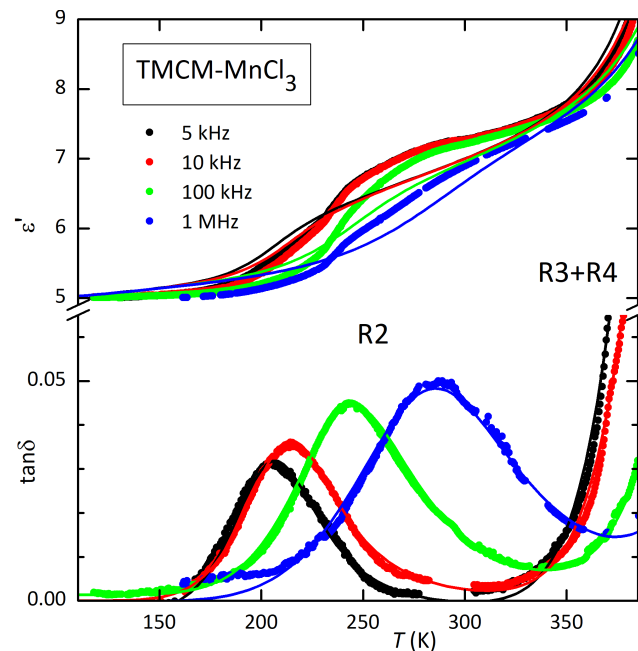
Figure 9. Global fit (thin lines) of the dielectric spectra of TMCM-MnCl$_3$ measured during cooling, with the same set of parameters for all frequencies. R2 is fit with Equations (2) and (3) with $\tau_0 = 2.6 \times 10^{-13}$ s, $E = 4100$ K, $\alpha = 0.77$, $\gamma = 0.65$, and $A = 650$ K.

In order to fit the high-temperature side of the spectrum, a completely phenomenological approach was adopted, due to the difficulty of reproducing R3, R4, the step-like anomaly at T_C, and possible other contributions. Therefore, the losses were fit by introducing an additional relaxation, which contributes little to ε'. The latter is approximately $\propto f^{1/2}$

above T_C, and we introduced the following background for ε': $\varepsilon_0 + \varepsilon_1 / \left[(T_C - T)^n f^{1/2} \right]$, limiting the fit enough below T_C. The result is the continuous lines in Figure 9, obtained with the following parameters for R2: $\tau_0 = 2.6 \times 10^{-13}$ s, $E = 4100$ K (corresponding to an activation energy 0.35 eV), $\alpha = 0.77$, $\gamma = 0.65$, $A = 650$ K (corresponding to 56 meV). The fit was optimised for $\tan \delta$, which is perfectly reproduced, while the step in ε' was underestimated. The main reason for the impossibility of fitting both real and imaginary parts is presumably the inability of the Havriliak–Negami distribution of the relaxation times to approximate the real one. Another approximation made is that the relaxation times are broadly distributed, but uncorrelated, each following the Arrhenius law, but it does not seem to be a major simplification. In fact, the value of τ_0 is typical for uncorrelated point defects, rather than extended defects ($\tau_0 > 10^{-12}$ s) or cooperative dynamics ($\tau_0 \ll 10^{-14}$ s and larger effective activation energy). Notice that $\overline{\tau}(T)$ at the maximum does not coincide with $1/(2\pi f)$, as usually assumed in the Arrhenius plots, because of the additional temperature dependence of the thermodynamic factor, Equation (3). In fact, in Figure 8, the $1/(2\pi\overline{\tau})$ line does not pass exactly through the black points, but it is anyway close to them.

It seems, therefore, that R2 is due to point defects' relaxation, but before discussing this point, let us consider the fit of the anelastic spectrum of TMCM-Mn$_{0.95}$Fe$_{0.05}$Cl$_3$ (Figure 5).

Those data are presented together with the fitting lines in Figure 10. In the logarithmic scale of Figure 5, the tail of R1 at a low temperature is evident, which was included in the fit. The fitting function was, therefore, the sum of three relaxations, each using Equation (2), but to reduce the number of parameters, for R1 and R3, γ was set to 1 and the asymmetry A to 0. Equation (2) is for susceptibility, which in the elastic case is the compliance $s = E^{-1}$. The fitting function was, therefore, the reciprocal of $s = s_0 + \Delta s_1 + \Delta s_2 + \Delta s_3$, where Δs_3 is included for improving the linear background of the imaginary part. The background of the real part was

$$s_0' = [M_0 - M_1 \tanh(\Theta/T)]^{-1},$$

which describes the linear stiffening of the solid during cooling, due to anharmonic effects, with quantum saturation below Θ [32]. The fitting parameters of R2 are: $\tau_0 = 1.4 \times 10^{-12}$ s, $E = 3830$ K, $\alpha = 0.94$, $\gamma = 0.55$, and $A = 400$ K, in fair agreement with those from the dielectric spectrum. The relaxation time extrapolated to infinite temperature, τ_0, is five-times larger and the borderline between point and extended defects, but it is less reliable, being deduced from two frequencies differing by a factor 5.5, whereas the dielectric curves span over three orders of magnitude of frequency. The activation energy is the same within 7%; the broadening parameters and the asymmetry energy are substantially similar to those of the dielectric curves, indicating that the same microscopic mechanism gives rise to R2 in the dielectric and anelastic spectra, and the partial substitution of Mn with Fe does not have a major effect on R2. Relaxation R1 has parameters $\tau_0 = 1 \times 10^{-13}$ s, $E = 1470$ K, and $\alpha = 0.9$, typical of point defects. Its presence is unnoticed in the linear scale of Q^{-1}, but not in the real part, since it produces a substantial softening with respect to the $E(T)$ baseline (dashed) still above 100 K. The parameters used for R3, $\tau_0 = 3 \times 10^{-15}$ s, $E = 14{,}400$ K, and $\alpha = 0.3$, are of no interest, since R3 was used as a background taking into account R3, R4, and anything else.
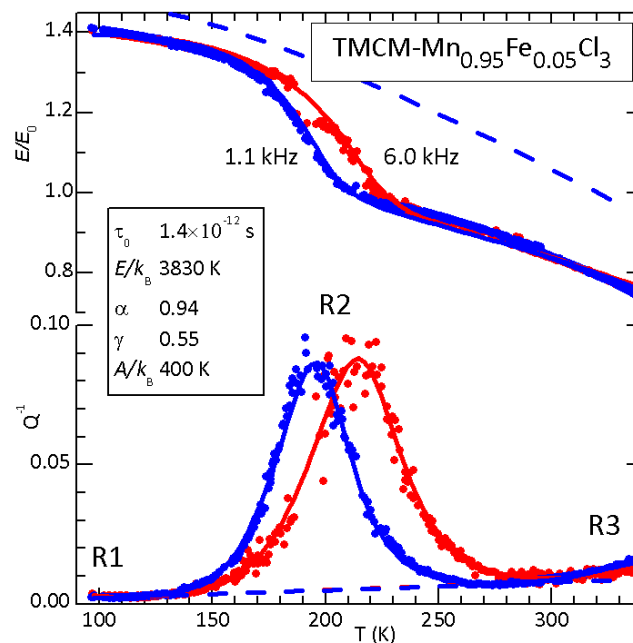
Figure 10. Global fit (solid lines) of the anelastic spectra of TMCM-$Mn_{0.95}Fe_{0.05}Cl_3$ measured during cooling, with the same set of parameters for all frequencies, as indicated in the legend and text. The dashed lines are the backgrounds obtained setting the amplitudes of R1–R3 to zero.

4.1. Tentative Identifications of the Microscopic Mechanisms of the Relaxations

There are at least four relaxation processes both in the dielectric and anelastic spectra, with activation energies spanning a range from 0.12 eV to >1 eV, therefore due to quite different mechanisms. Let us start with the highest activation energy.

4.1.1. R4 and the Grain Boundary Relaxation

If R4 were observed only in the dielectric susceptibility, it would be natural to ascribe it to the space charge arising from ionised defects, such as the TMCM and Cl vacancies, which must be abundant. Indeed, the strong rise of the dielectric susceptibility with decreasing frequency suggests that a considerable contribution of the space charge is present, but R4 is also observed in the anelastic spectra, which are insensitive to the space charge. Therefore, R4 must contain a contribution from another mechanism involving also strain. Considering that these hybrid metallorganic perovskites start decomposing at rather low temperature, below 500 K, it seems reasonable to ascribe R4 to grain boundary relaxation. The motion of grain boundaries involves the diffusion of all atoms and the breaking and formation of covalent bonds of the $MnCl_3$ backbone, and therefore, it is expected to be the relaxation process with the largest activation energy and distribution of relaxation times. The tail of the R4 relaxation probably continues below T_C, little affected by the structural transformation.

4.1.2. Domain wall Relaxation and R3

The step in the losses when crossing T_C is due to the motion of the walls between the domains of the different variants of the low-temperature phase. Furthermore, the domain wall relaxation is usually a very broad process, due to the distribution of domain sizes, morphologies, and pinning of the wall motion by point defects and grain boundaries. It seems reasonable to assign also R3 to domain wall relaxation, which often exhibits a thermally activated maximum below the transition temperature [33–35]. We did not find, however, an evident relationship between the magnitude of R3 and the type of Mn substitution. Usually, the presence of impurities and defects pins the motion of the walls, which means blocking the walls or increasing their relaxation time. This causes a suppression of the peak height and/or a shift of the relaxation maximum at a higher temperature, possibly higher than T_C, where, however, the walls disappeared. If the

substitutional atoms are pinning centres for the domain walls, then it is not immediately clear why the undoped material has the lowest R3. Probably, this type of substitution does not constitute a major disturbance of the lattice, and this is promising from the perspective of exploring these solid solutions.

4.1.3. Reorientation of the TMCM Molecule and Associated Elastic Dipole

We considered now the possible types of defect relaxations that may give rise to R2 and R1. We started by considering the residual reorientation of single TMCM molecules in the ferroelectric phase, since this type of motion has been argued to cause a similar intense relaxation process in another molecular perovskite: the anelastic spectrum of MAPbI$_3$ (MA = Methylammonium) contains an extremely intense thermally activated relaxation, with associated softening of ∼50% in Young's modulus [25,26], with an activation energy of 0.20 eV and broadening parameters, which are intermediate between R1 and R2. The anelastic relaxation in MAPbI$_3$ has no dielectric counterpart and has been interpreted in terms of the reorientation of pairs of MA molecules with the opposite direction of the polarisation, therefore having an elastic, but not a dielectric dipole. In fact, in spite of numerous reports that the low-temperature phases of MAPbI$_3$ are ferroelectric due to the ordering of the MA dipoles, in the γ phase, where the anelastic relaxation is observed, there appear to be antiferroelectric correlations and residual degrees of freedom of the MA molecules within the *ab* plane [25,26]. In spite of some similarities between MAPbI$_3$ and TMCM-MnCl$_3$, a similar mechanism does not seem appropriate to explain R2. In fact, in order to explain the large amplitude of R2 in terms of the reorientation of the TMCM molecules, it would be necessary to assume that their major axis, approximately parallel to their electric dipole, changes direction, in order to have a sufficiently large change of the elastic dipole tensor (deformation ellipsoid shown in blue in Figure 11). In fact, the relaxation strength Δ of n point defects per mole that change their the elastic dipole of $\Delta\lambda$ during reorientation is $\Delta \propto n(\Delta\lambda)^2/T$ [21]. Different from cubic MAPbI$_3$, where the MA molecules may reorient their major axis of 90° [36] with a consequent large $\Delta\lambda$, the TMCM in TMCM-MnCl$_3$ is always oriented almost parallel to the *c* crystal axis, with a minor change of the elastic dipole during the fast threefold rotation around *c* (Figure 11b) and no change during a flip of the electric dipole by 180° (Figure 11a). Therefore, the rotational motion of TMCM cannot produce major anelastic relaxation, and we should consider other types of point defects.
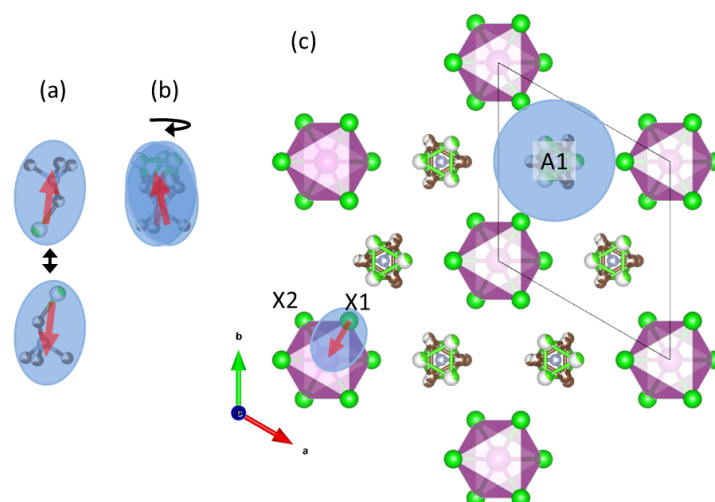

Figure 11. (**a**) TMCM molecule that reorients its major axis of 180°, reorienting its electric dipole (red arrow) in the same manner, but leaving the elastic dipole (blue ellipsoid) unchanged; (**b**) rotation of 120° of the TMCM molecule around its major axis, with little change in electric and elastic dipoles; (**c**) TMCM vacancy in site A1, with no electric dipole and elastic dipole that is isotropic within the *ab* plane; a Cl vacancy in X1 forms an electric and elastic dipole with one or both of its nearest neighbour Mn atoms along the *c* axis.

4.1.4. Isotropic TMCM Vacancy and Anisotropic Cl Vacancy: A Possible Contribution to R1

Certainly, the most-abundant defects in the molecular perovskites ABX_3, with A an organic molecule, are the A and X vacancies (V_A and V_X). Similar to cubic perovskites, the activation energy for hopping of V_A will be larger than that of V_X, and the hopping of an isolated V_A causes neither dielectric, nor anelastic relaxation. This is clear from Figure 11c, where it appears that V_A does not break the C_3 symmetry of the A site and there is no privileged direction for creating an electric dipole or making the elastic dipole anisotropic within the *ab* plane.

On the other hand, an isolated V_X will affect the electronic state of one or both of its nearest neighbour Mn atoms along the MnX_3 column, creating an electric dipole and making the elastic dipole anisotropic with the major (or minor; this is inessential) axis along the same direction (Figure 11c). A jump of V_{Cl} from X1 to X2 or any of the four nearest neighbour X sites causes a reorientation of about 90° of the electric and elastic dipoles. Being the fastest among the point defect jumps, it may contribute to the relaxation process with the lowest activation energy, R1. Notice that, in cubic perovskites, the hopping of an isolated V_X does not produce dielectric relaxation, because it has two nearest neighbour B atoms in opposite directions, and no electric dipole is created [37]. Moreover, in the hexagonal perovskites with columns of BX_6 octahedra, V_X are bound to diffuse within the same column, unless the A cations support missing or excess X.

A final remark on the expected abundance of isolated V_X is due. In inorganic oxide perovskites, relatively large amounts of V_O can be reversibly created and eliminated with thermal treatments in reducing or O_2 atmospheres, without affecting the perovskite framework of metallic cations, and the hopping and clustering of V_O can, therefore, be observed [37]. In the hybrid metal–organic perovskites, there are no quantitative studies on the formation of these defects; however, the organic cations are certainly less stable than metallic A cations, and it is perhaps impossible to create V_X without an equal or even larger amount of V_A. It is therefore expected that V_{Cl} and V_{TMCM} are present in approximately equal amounts, as discussed below.

4.1.5. Pairs of TMCM and Cl Vacancies: R1 as Fast Reorientation through Cl Hopping

In $TMCM\text{-}MnCl_3$, the formal valences are +1 for A = TMCM, +2 for Mn, and −1 for Cl, so that the charge neutrality requires equal numbers of V_A and V_X. It is known that the formation energy of this type of Schottky defect is low in hybrid halide perovskites [38], and therefore, it is expected that the major species of defects are approximately equal amounts of V_{Cl} and V_{TMCM}, at least in the absence of strong electric fields [39]. At a low temperature, these defects will tend to combine in pairs, due to the electrostatic interaction, and therefore, we expect that the major species of defects below room temperature is V_A–V_X pairs. The geometry of such a pair is shown in Figure 12. If there is a V_{TMCM} in the A1 position and a V_{Cl} in the left $MnCl_3$ column, then V_{Cl} will preferentially reside in the nearest neighbour positions X1 and X2. The top view along the *c* axis of two possible pairs in Figure 12b demonstrates that the reorientation of the pair involves sizeable changes in the electric and elastic dipoles, and we argue that it should cause essentially two types of relaxation processes: a fast one associated with V_{Cl} hopping and a slower one due to V_{TMCM} hopping, respectively contributing to R1 and R2.

Indeed, the jumps of V_{Cl} between two equivalent positions with respect to V_{TMCM} would be fast and, therefore, would contribute to R1, as suggested in the previous subsection, with the difference that a V_X paired with a V_A would probably affect the neighbouring B cations less than an isolated V_X. Therefore, the effect of V_X hopping within a V_A–V_X pair should be seen as in Figure 13a. The identification of R1 as due to V_{Cl} jumps is in agreement with the literature, since its estimated activation energy of 0.13 eV is in the lower part of the extremely wide range 0.08–0.7 eV of the activation energies for the hopping of halide vacancies in perovskites [40] measured by impedance spectroscopy [41], NMR relaxation [42], current–voltage curves [43], and DFT calculations [40]. Together with NMR relaxation experiments, the dielectric and anelastic spectra provide the most-reliable mea-

surements of the hopping rates of vacancies and point defects, but further measurements are necessary to confirm the identification of R2 and R1 with the jumps of the TMCM and Cl vacancies.
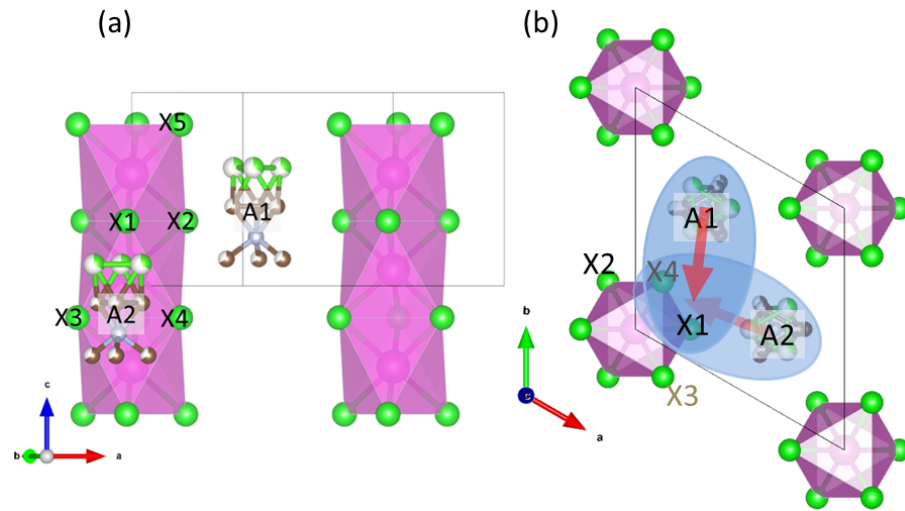

Figure 12. Geometry of the pair of TMCM and Cl vacancies. (**a**) Side view of a TMCM vacancy in A1, with the Cl vacancy preferentially occupying its nearest neighbour X1 and X2 sites; after a jump of the TMCM vacancy to A2, the Cl vacancy will visit preferentially the X3 and X4 sites. (**b**) Top view with representation of the electric and elastic dipoles associated with vacancy pairs in A1 and X1 and in A2 and X4.

relaxation R1:
$$V_{A1}\text{-}V_{X1} \leftrightarrow V_{A1}\text{-}V_{X2}$$

relaxation R2:
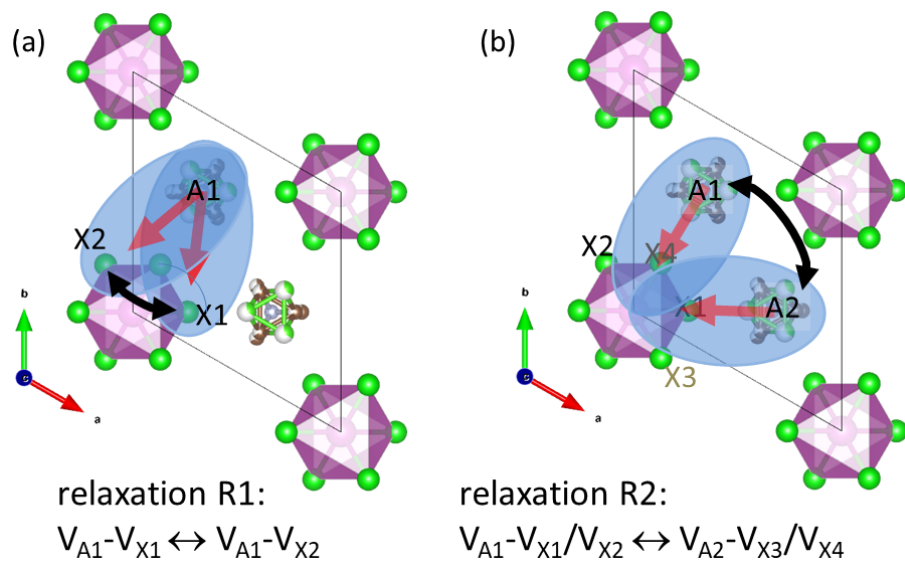$$V_{A1}\text{-}V_{X1}/V_{X2} \leftrightarrow V_{A2}\text{-}V_{X3}/V_{X4}$$

Figure 13. Proposed main contributions to relaxations R1 and R2.

4.1.6. Pairs of TMCM and Cl Vacancies: R2 as Slow Reorientation through TMCM Hopping

On the slower time scale of TMCM vacancy hopping, the electric and elastic dipoles of the V_A–V_X pair appear as averages between the two equivalent X positions, as shown in Figure 13b. This type of jump, slower than that of V_{Cl}, seems the best candidate for the major dielectric and anelastic relaxation process with the characteristics of point defects, namely R2.

4.1.7. Width of the Relaxation Peaks and Multiplicity of Defect Complexes in the Hexagonal Perovskite

Finally, we comment on the fact that R2, even though identified with point defect relaxation, is considerably broader than a Debye relaxation. For comparison, in the cubic perovskite oxide $SrTiO_{3-\delta}$, isolated V_O diffuse with an activation energy of 0.60 eV, while the reorientation of pairs of V_O requires 1.0 eV, and both the anelastic relaxation peaks are close to single-time Debye relaxations ($\alpha \geq 0.95$), at least up to $\delta \sim 0.01$ [37]. The point is that, in hexagonal perovskites with large molecular A cations, the distances between A and X are larger than in cubic perovskites, and due to the columnar geometry of the BX_6 octahedra, there are several X sites facing an A site with distances that differ little from each other. The distance between A1 and its 2nd neighbours X4 and X5 is only 9% larger than that to the 1st neighbours X1 and X2 (Figure 12), whereas in the cubic structure, it is 73% larger. In addition, the asymmetry of TMCM and its possible shift along the *c* axis in the ferroelectric phase make the sites X4 and X5 non-equivalent with respect to its vacancy in A1. Therefore, at variance with the cubic structure, there is a large number of pairs of vacancies differing relatively little in energy, A1–X1/X2, A1–X4, and A1–X5, whose populations will also be comparable. They will have slightly different dipoles and activation energies, producing multiple relaxation peaks, difficult to distinguish from a single broad peak. Then, the large widths of the relaxation peaks R2 and R1 do not necessarily imply a very high concentration of vacancies or particularly defective lattice; they are a consequence of the geometry of the 1D hexagonal perovskite structure, which allows the existence of several types of defect jumps and pairs with small differences between each other, appearing as a single broad relaxation.

4.2. Absorption of Humidity

In the SI, it is shown that the ammonium salt TMCM-Cl is extremely hygroscopic, becoming a liquid in minutes after staying in air with 33% relative humidity (RH). The powder of $TMCM-MnCl_3$, instead, is much more stable, and under the same conditions, does not present any sign of absorption of humidity after 2 h. When weighted with a microbalance in air with 70% RH, no mass gain was observed at least for several minutes. On the contrary, after being pressed at 0.3–0.4 GPa for a few minutes, the compacted powder promptly condensed water from humidity on the surface, when it was not already wet, and attached to the metal pressing pieces immediately after being extracted from the die. Apparently, the surface of the crystalline particles promptly adsorbs water from humidity; however, after an initial saturation of the surface, there is no further condensation, and probably, water does not intercalate into the lattice. During pressing, which we cannot exclude makes the phase partially fluid, the water adsorbed on the surfaces of the crystallites partly intercalated into the bulk and partly went to the surface, making the pressed sample wet. Exposure of the compacted sample to humid air was accompanied by further condensation of water, and this can be explained assuming that the grain boundaries are strong centres for water condensation and probably absorption into the bulk.

These observations are closely related to those made in the other molecular perovskite $FAPbI_3$ [15,44]. Furthermore, the loose powder of FAPI can withstand exposure to humid air without appreciable degradation for over three months, but the compacted powder is degraded within one day, unless kept in a vacuum. With FAPI, the situation is complicated by the fact that it has several polymorphs with energies close to each other at room temperature and, therefore, metastable: from the cubic black perovskite to the most-stable hexagonal yellow phase, identical to that of $TMCM-MnCl_3$, passing through a series of phases with mixed connectivity of the PbI_6 octahedra and intermediate orange colours [15,45]. Because of these phenomena, it has been shown by anelastic and dielectric spectroscopy that, in FAPI, the water molecules intercalate into the lattice and favour the transformation from the metastable cubic phase to the hexagonal one and further promote decomposition with the loss of FA-I [15,44,46].

Apparently, TMCM-MnCl$_3$ is not decomposed by intercalated water and does not undergo the structural rearrangements of cubic FAPI into various polymorphs, because it is already in the stable structure with parallel columns of octahedra. In fact, the initially wet pressed powder, once dried, exhibits the dielectric and anelastic properties expected from TMCM-MnCl$_3$, starting from the transition at 400 K. In addition, the powder can be synthesised from aqueous solution and again dispersed in water and quickly frozen, to be successfully deposited by MAPLE into films, whose piezoelectric activity was verified with PFM. Yet, the powder pressed in air with relative humidity >50% contained a considerable amount of water intercalated within the bulk, even when thoroughly dried in a high vacuum and exposed to humidity only a few minutes before pressing. This is apparent from the initial stage of the anelastic experiments, where the sample was mounted immediately after application of the Ag electrode. The loss of water started immediately after closing the system, which was in a high vacuum, and proceeded for hours at room temperature. During this stage, the elastic modulus increased 40% and perhaps more. We have no quantitative data, because the stiffening rate decreased rapidly with time, and the initial stage was lost in adjustments and searching the resonances. Yet, an increase of Young's modulus of the order of 40% cannot be due to water adsorbed at the surface or to the initial consolidation of the Ag paint of the electrode; it must be due to water intercalated within the bulk, which can outdiffuse fast in the high vacuum environment.

The adverse effect of humidity seems to be on the cohesion of the grains rather than on their composition, at least at an initial stage. The effect was particularly evident on the pressed bars of the anelastic experiments. The samples of TMCM-Mn$_{0.95}$Fe$_{0.05}$Cl$_3$ were dry after pressing; the bar was measured as shown in Figure 5 and left in a static vacuum, remaining intact without changing Young's modulus for a month, after which, it was exposed to air for some minutes and again evacuated. After 6 days, the surface was completely flaked, as also observed in other bars after being measured (Figure S5c). This fact suggests an adverse effect of water on cohesion, presumably due to a volume expansion of the hydrated material, in addition to a weakening of the bonds between TMCM and the columns of the MnCl$_6$ octahedra. The same mechanism might be operative in polycrystalline films, though we did not observe the degradation of the films deposited with MAPLE, while nothing of the kind has been reported for single crystals, which do not have grain boundaries as coalescence centres for humidity.

5. Conclusions

Powders of the hexagonal perovskite TMCM-MnCl$_3$ and TMCM-Mn$_{0.95}$M$_{0.05}$Cl$_3$, M = Cu, Ni, and Fe, were prepared and pressed into bars and pellets and deposited as films by matrix-assisted pulsed laser evaporation. The films were characterised by PFM, finding the signatures of piezoelectrically active domains. The samples of the pressed powders were used for measuring the dielectric susceptibility and the complex Young's modulus. The dielectric and anelastic spectra were very consistent with each other and, besides jumps in the susceptibilities due to the improper ferroelectric transition, contained four relaxation processes, both dielectric and anelastic. The two partially overlapping processes at higher temperature were tentatively assigned to grain boundary and domain wall relaxations, and their intensities were enhanced by Mn substitution with Cu and Fe. The other two relaxation processes were interpreted in terms of point defects, after extracting their relaxation parameters from the global fits of the real and imaginary parts of the dielectric and anelastic spectra at different frequencies. It is argued that, below room temperature, the major species of point defects should be pairs of Cl and TMCM vacancies, having both electric and elastic dipoles. Their reorientation is possible through Cl hopping on a fast time scale, contributing to relaxation R1 with the lowest activation energy of ∼0.13 eV, and through TMCM hopping on a slower time scale, contributing to the major relaxation R2 with an activation energy of 0.34 ± 0.01 eV. Peak R2 is very broad, and this was interpreted noting that, at variance with the cubic perovskite, in the hexagonal perovskite structure, the distances between a TMCM site and the Cl sites up to the forth neighbour differ only

slightly from each other. Peak R2 would therefore be a superposition of the relaxations from various configurations of vacancy pairs, which differ slightly in distance and in the relaxation parameters.

It was observed that, while the loose powder of doped and undoped TMCM-MnCl$_3$ did not appear to be degraded by exposure to humid air, samples compacted by cold pressing promptly condensed water on their surface. This was attributed to a tendency of grain boundaries to act as coalescence centres for water, similar to other organic–inorganic perovskites, such as FAPbI$_3$, and caused a loss of cohesion between the grains.

References

1. Lines, M.E.; Glass, A.M. *Principles and Applications of Ferroelectrics and Related Materials*; Oxford University Press: Oxford, UK, 1977.
2. Rödel, J.; Jo, W.; Seifert, K.P.; Anton, E.M.; Granzow, T.; Damjanovic, D. Perspective on the Development of Lead-free Piezoceramics. *J. Am. Ceram. Soc.* **2009**, *92*, 1153–1177. [CrossRef]
3. Moure, A. Review and Perspectives of Aurivillius Structures as a Lead-Free Piezoelectric System. *Appl. Sci.* **2018**, *8*, 62. [CrossRef]
4. Wendari, T.P.; Arief, S.; Mufti, N.; Blake, G.R.; Baas, J.; Suendo, V.; Prasetyo, A.; Insani, A.; Zulhadjri, Z. Lead-Free Aurivillius Phase Bi$_2$LaNb$_{1.5}$Mn$_{0.5}$O$_9$: Structure, Ferroelectric, Magnetic, and Magnetodielectric Effects. *Inorg. Chem.* **2022**, *61*, 8644–8652. [CrossRef]
5. Liao, W.Q.; Zhao, D.; Tang, Y.Y.; Zhang, Y.; Li, P.F.; Shi, P.P.; Chen, X.G.; You, Y.M.; Xiong, R.G. A molecular perovskite solid solution with piezoelectricity stronger than lead zirconate titanate. *Science* **2019**, *363*, 1206–1210. [CrossRef] [PubMed]
6. Liao, W.Q.; Tang, Y.Y.; Li, P.F.; You, Y.M.; Xiong, R.G. Competitive Halogen Bond in the Molecular Ferroelectric with Large Piezoelectric Response. *J. Am. Chem. Soc.* **2018**, *140*, 3975–3980. [CrossRef]
7. You, Y.M.; Liao, W.Q.; Zhao, D.; Ye, H.Y.; Zhang, Y.; Zhou, Q.; Niu, X.; Wang, J.; Li, P.F.; Fu, D.W.; et al. An organic-inorganic perovskite ferroelectric with large piezoelectric response. *Science* **2017**, *357*, 306–309. [CrossRef] [PubMed]
8. Li, W.; Wang, Z.; Deschler, F.; Gao, S.; Friend, R.H.; Cheetham, A.K. Chemically diverse and multifunctional hybrid organic-inorganic perovskites. *Nat. Rev. Mater.* **2017**, *2*, 16099. [CrossRef]
9. Liu, H.Y.; Zhang, H.Y.; Chen, X.G.; Xiong, R.G. Molecular Design Principles for Ferroelectrics: Ferroelectrochemistry. *J. Am. Chem. Soc.* **2020**, *142*, 15205–15218. [CrossRef]
10. Pan, Q.; Xiong, Y.A.; Sha, T.T.; You, Y.M. Recent progress in the piezoelectricity of molecular ferroelectrics. *Mater. Chem. Front.* **2021**, *5*, 44–59. [CrossRef]
11. Han, X.B.; Chai, C.Y.; Liang, B.D.; Fan, C.C.; Zhang, W. Ferroic phase transition molecular crystals. *CrystEngComm* **2022**, *24*, 1507–1517 . [CrossRef]
12. Burtch, N.C.; Heinen, J.; Bennett, T.D.; Dubbeldam, D.; Allendorf, M.D. Mechanical Properties in Metal-Organic Frameworks: Emerging Opportunities and Challenges for Device Functionality and Technological Applications. *Adv. Mater.* **2018**, *30*, 1704124. [CrossRef] [PubMed]
13. Lee, J.W.; Park, N.G. Chemical Approaches for Stabilizing Perovskite Solar Cells. *Adv. Energy Mater.* **2020**, *10*, 1903249. [CrossRef]
14. Huang, H.; Pradhan, B.; Hofkens, J.; Roeffaers, M.J.; Steele, J.A. Solar-Driven Metal Halide Perovskite Photocatalysis: Design, Stability, and Performance. *ACS Energy Lett.* **2020**, *5*, 1107–1123. [CrossRef]
15. Cordero, F.; Craciun, F.; Trequattrini, F.; Generosi, A.; Paci, B.; Paoletti, A.M.; Zanotti, G. Influence of Temperature, Pressure, and Humidity on the Stabilities and Transition Kinetics of the Various Polymorphs of FAPbI$_3$. *J. Phys. Chem. C* **2020**, *124*, 22972. [CrossRef]

16. Alin, C.D.; Grama, F.; Papagheorghe, R.; Brajnicov, S.; Ion, V.; Vizireanu, S.; Palla-Papavlu, A.; Dinescu, M. Tuning the physicochemical properties of hernia repair meshes by matrix-assisted pulsed laser evaporation. *Appl. Phys. A* **2019**, *125*, 424. [CrossRef]

17. Zhang, Z.; Li, W.; Carpenter, M.A.; Howard, C.J.; Cheetham, A.K. Elastic properties and acoustic dissipation associated with a disorder-order ferroelectric transition in a metal-organic framework. *CrystEngComm* **2015**, *17*, 370–374. [CrossRef]

18. Cordero, F. Elastic Properties and Enhanced Piezoelectric Response at Morphotropic Phase Boundaries. *Materials* **2015**, *8*, 8195–8245. [CrossRef]

19. Davies, W.C.; Evans, E.B.; Hulbert, F.L. 92. The formation of quaternary ammonium salts from dihalogenoparaffins, etc., in aqueous acetone solution. *J. Chem. Soc.* **1939** , 412–418. [CrossRef]

20. Cordero, F.; Bella, L.D.; Corvasce, F.; Latino, P.M.; Morbidini, A. An insert for anelastic spectroscopy measurements from 80 K to 1100 K. *Meas. Sci. Technol.* **2009**, *20*, 015702. [CrossRef]

21. Nowick, A.S.; Berry, B.S. *Anelastic Relaxation in Crystalline Solids*; Academic Press: New York, NY, USA, 1972.

22. Rehwald, W. The Study of Structural Phase Transitions by Means of Ultrasonic Experiments. *Adv. Phys.* **1973**, *22*, 721–755. [CrossRef]

23. Cordero, F.; Craciun, F.; Trequattrini, F.; Galassi, C. Piezoelectric softening in ferroelectrics: Ferroelectric versus antiferroelectric $PbZr_{1-x}Ti_xO_3$. *Phys. Rev. B* **2016**, *93*, 174111. [CrossRef]

24. Cordero, F. Piezoelectricity from Elastic and Dielectric Measurements on Unpoled Ferroelectrics. *Mater. Res.* **2018**, *21* (Suppl. 2), e20170852. [CrossRef]

25. Cordero, F.; Craciun, F.; Trequattrini, F.; Imperatori, P.; Paoletti, A.M.; Pennesi, G. Competition between Polar and Antiferrodistortive Modes and Correlated Dynamics of the Methylammonium Molecules in MAPbI$_3$. *J. Phys. Chem. Lett.* **2018**, *9*, 4401–4406. [CrossRef]

26. Cordero, F.; Trequattrini, F.; Craciun, F.; Paoletti, A.M.; Pennesi, G.; Zanotti, G. Cation reorientation and octahedral tilting in the metal-organic perovskites MAPI and FAPI. *J. Alloy Compd.* **2021**, *867*, 158210. [CrossRef]

27. Havriliak, S.; Negami, S. A complex plane analysis of α-dispersions in some polymer systems. *J. Poly. Sci. C* **1966**, *14*, 99–117. [CrossRef]

28. Sencadas, V.; Lanceros-Méndez, S.; Sabater i Serra, R.; Andrio Balado, A.; Gómez Ribelles, J.L. Relaxation dynamics of poly(vinylidene fluoride) studied by dynamical mechanical measurements and dielectric spectroscopy. *Eur. Phys. J. E* **2012**, *35*, 41. [CrossRef] [PubMed]

29. Nowick, A.S.; Heller, W.R. Dielectric and anelastic relaxation of crystals containing point defects. *Adv. Phys.* **1965**, *14*, 101–166. [CrossRef]

30. Nowick, A.S. Partial relaxation magnitudes for anelastic and dielectric relaxation due to point defects. *J. Phys. Chem. Sol.* **1970**, *34*, 1507–1521. [CrossRef]

31. Cordero, F. Anelastic (dielectric) relaxation of point defects at any concentration, with blocking effects and formation of complexes. *Phys. Rev. B* **1993**, *47*, 7674. [CrossRef]

32. Salje, E.; Wruck, B.; Thomas, H. Order-parameter saturation and low-temperature extension of Landau theory. *Z. Phys. B Condens. Matter* **1991**, *82*, 399–404. [CrossRef]

33. Arlt, G.; Dederichs, H.; Herbiet, R. 90°-domain wall relaxation in tetragonally distorted ferroelectric ceramics. *Ferroelectrics* **1987**, *74*, 37–53. [CrossRef]

34. Wang, Y.N.; Tian, W.; Huang, Y.N.; Yan, F.; Shen, H.M.; Zhu, J.S.; Zhang, Z.F. Mechanical and dielectric dissipation related to phase transitions. *Phase Transit.* **2000**, *72*, 57–80. [CrossRef]

35. Yadav, P.; Sharma, S.; Lalla, N.P. Coexistence of domain relaxation with ferroelectric phase transitions in BaTiO$_3$. *J. Appl. Phys.* **2017**, *121*, 184101. [CrossRef]

36. Chen, T.; Foley, B.J.; Ipek, B.; Tyagi, M.; Copley, J.R.; Brown, C.M.; Choi, J.J.; Lee, S.H. Rotational dynamics of organic cations in the CH$_3$NH$_3$PbI$_3$ perovskite. *Phys. Chem. Chem. Phys.* **2015**, *17*, 31278. [CrossRef] [PubMed]

37. Cordero, F. Hopping and clustering of oxygen vacancies in SrTiO$_3$ by anelastic relaxation. *Phys. Rev. B* **2007**, *76*, 172106. [CrossRef]

38. Walsh, A.; Scanlon, D.O.; Chen, S.; Gong, X.G.; Wei, S.H. Self-Regulation Mechanism for Charged Point Defects in Hybrid Halide Perovskites. *Angew. Chem. Int. Ed.* **2015**, *54*, 1791. [CrossRef] [PubMed]

39. Birkhold, S.T.; Precht, J.T.; Giridharagopal, R.; Eperon, G.E.; Schmidt-Mende, L.; Ginger, D.S. Direct Observation and Quantitative Analysis of Mobile Frenkel Defects in Metal Halide Perovskites Using Scanning Kelvin Probe Microscopy. *J. Phys. Chem. C* **2018**, *24*, 12633. [CrossRef]

40. Barboni, D.; Souza, R.A.D. The Thermodynamics and Kinetics of Iodine Vacancies in the Hybrid Perovskite Methylammonium Lead Iodide. *Energy Environ. Sci.* **2018**, *11*, 3266–3274. [CrossRef]

41. Mizusaki, J.; Arai, K.; Fueki, K. Ionic conduction of the perovskite-type halides. *Solid State Ion.* **1983**, *11*, 203–211. [CrossRef]

42. Kubicki, D.J.; Prochowicz, D.; Salager, E.; Rakhmatullin, A.; Grey, C.P.; Emsley, L.; Stranks, S.D. Local structure and dynamics in methylammonium, formamidinium and cesium tin(II) mixed-halide perovskites from 119Sn solid-state NMR. *J. Am. Chem. Soc.* **2020**, *142*, 7813–7826. [CrossRef]

43. Karimata, I.; Tachikawa, T. In Situ Exploration of the Structural Transition during Morphologyand Efficiency-Conserving Halide Exchange on a Single Perovskite Nanocrystal. *Angew. Chem. Int. Ed.* **2020**, *133*, 2578–2583. [CrossRef]

44. Cordero, F.; Craciun, F.; Trequattrini, F.; Generosi, A.; Paci, B.; Paoletti, A.M.; Pennesi, G. Stability of Cubic FAPbI$_3$ from X-ray Diffraction, Anelastic, and Dielectric Measurements. *J. Phys. Chem. Lett.* **2019**, *10*, 2463–2469. [CrossRef] [PubMed]

45. Gratia, P.; Zimmermann, I.; Schouwink, P.; Yum, J.H.; Audinot, J.N.; Sivula, K.; Wirtz, T.; Nazeeruddin, M.K. The Many Faces of Mixed Ion Perovskites: Unraveling and Understanding the Crystallization Process. *ACS Energy Lett.* **2017**, *2*, 2686–2693. [CrossRef]

46. Boyd, C.C.; Cheacharoen, R.; Leijtens, T.; McGehee, M.D. Understanding Degradation Mechanisms and Improving Stability of Perovskite Photovoltaics. *Chem. Rev.* **2019**, *119*, 3418–3451. [CrossRef]

47. Salaken, S.M.; Farzana, E.; Podder, J. Effect of Fe-doping on the structural and optical properties of ZnO thin films prepared by spray pyrolysis. *J. Semicond.* **2013**, *34*, 073003. [CrossRef]

48. Liao, W.Q.; Gao, J.X.; Hua, X.N.; Chen, X.G.; Lu, Y. Unusual two-step sequential reversible phase transitions with coexisting switchable nonlinear optical and dielectric behaviors in [(CH$_3$)$_3$NCH$_2$Cl]$_2$[ZnCl$_4$]. *J. Mater. Chem. C* **2017**, *5*, 11873–11878. [CrossRef]

49. Hua, X.N.; Huang, C.R.; Gao, J.X.; Lu, Y.; Chen, X.G.; Liao, W.Q. High-temperature reversible phase transitions and exceptional dielectric anomalies in cobalt(ii) based ionic crystals: [Me$_3$NCH$_2$X]$_2$[CoX$_4$] (X = Cl and Br). *Dalton Trans.* **2018**, *47*, 6218–6224. [CrossRef]

50. Hua, X.N.; Liao, W.Q.; Tang, Y.Y.; Li, P.F.; Shi, P.P.; Zhao, D.; Xiong, R.G. A Room-Temperature Hybrid Lead Iodide Perovskite Ferroelectric. *J. Am. Chem. Soc.* **2018**, *140*, 12296–12302. [CrossRef]